ACS APPLIED MATERIALS & INTERFACES

www.acsami.org

Research Article

A Near-Infrared Emitting Aggregation-Induced Emission Photosensitizer with Endoplasmic Reticulum Targeting Ability for Breast Cancer Photodynamic Therapy

Zeeshan Tahir, Sayed Mir Sayed,* Elif Lulek, Zehra Busra Azizoglu, Gulce Yildiz, Esra Balcioglu, Aysun Cetin,* and Yavuz Nuri Ertas*

Cite This: *ACS Appl. Mater. Interfaces* 2026, 18, 13516−13528

Read Online

ACCESS | Metrics & More | Article Recommendations | Supporting Information

ABSTRACT: Organelle-specific photosensitizers offer an effective strategy to enhance photodynamic therapy (PDT) by spatially confining reactive oxygen species (ROS) generation to vulnerable intracellular sites; however, most conventional photosensitizers suffer from aggregation-caused quenching (ACQ), limited subcellular targeting precision, and inefficient ROS generation under low-intensity visible or white light irradiation. Herein, we report a naphthalimide-based aggregation-induced emission (AIE) photosensitizer, TPAPV-NIM-TSA, rationally engineered to address these limitations through endoplasmic reticulum (ER) targeting, near-infrared (NIR) fluorescence imaging, and efficient photodynamic tumor ablation. Encapsulation of TPAPV-NIM-TSA within a Pluronic F127 matrix yields stable nanoparticles (TPAPV-NIM-TSA@F127) with improved aqueous dispersibility, biocompatibility, and cellular uptake. The donor−π−acceptor molecular architecture with extended π-conjugation results in broad visible-light absorption and a reduced singlet−triplet energy gap, as supported by density functional theory calculations, enabling efficient intersystem crossing and the simultaneous generation of both type I and type II ROS under low-intensity white light irradiation. TPAPV-NIM-TSA@F127 exhibits pronounced AIE behavior with NIR fluorescence emission, facilitating intracellular imaging while avoiding ACQ. Confocal microscopy and colocalization analyses confirm selective accumulation of TPAPV-NIM-TSA@F127 in the ER, where ER-localized ROS generation leads to effective photodynamic ablation of breast cancer cells with minimal dark toxicity. In vivo evaluation in 4T1 tumor-bearing BALB/c mice demonstrates significant tumor growth inhibition and near-complete tumor eradication under white light irradiation, accompanied by negligible systemic toxicity, minimal hemolysis, and no observable damage to major organs. These results establish TPAPV-NIM-TSA@F127 as a multifunctional ER-targeted AIE photosensitizer that integrates imaging capability, dual ROS generation pathways, and effective in vivo PDT, providing a promising platform for the development of next-generation organelle-targeted phototherapeutic materials.

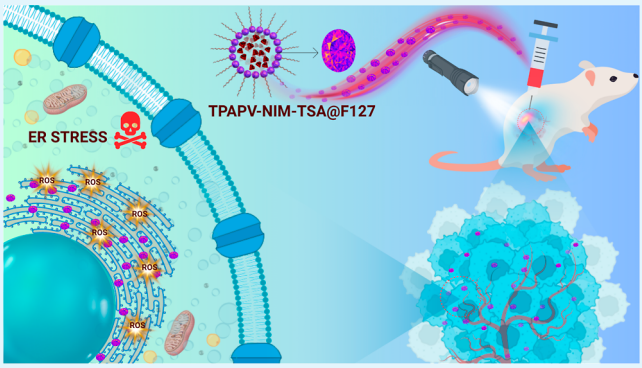

KEYWORDS: *aggregation-induced emission, reactive oxygen species (ROS), NIR emission, endoplasmic reticulum targeting, breast cancer, photodynamic therapy*

1. INTRODUCTION

Cancer, with an anticipated 13.1 million fatalities by 2030, remains a leading cause of mortality worldwide, accounting for approximately one in six deaths globally and posing a significant burden on public health.[1,2] Innovative and effective treatment options are in high demand due to the disease's high incidence rate. As a result, numerous conventional cancer treatment methods, including surgery, chemotherapy, and radiotherapy, have been implemented; however, these methods have certain drawbacks. For instance, in the context of surgery, the early detection of a tumor is a difficult task, and there is a possibility of recurrence. While chemotherapy and radiotherapy are capable of effectively eliminating cancer cells, the precise elimination of only cancer cells is unattainable, and they also cause significant side effects by killing and damaging adjacent normal cells.[3−7] To address these issues, it is crucial to selectively target cancer cells while minimizing damage to the nearby normal cells. Photodynamic therapy (PDT) is one of the most effective options for killing cancer cells, as it

Received: December 14, 2025
Revised: February 10, 2026
Accepted: February 10, 2026
Published: February 26, 2026

Scheme 1. Schematic Illustration of the Synthesis of TPAPV-NIM-TSA@F127 and ER-Targeted Light-Induced Ablation of Cancerous Cells

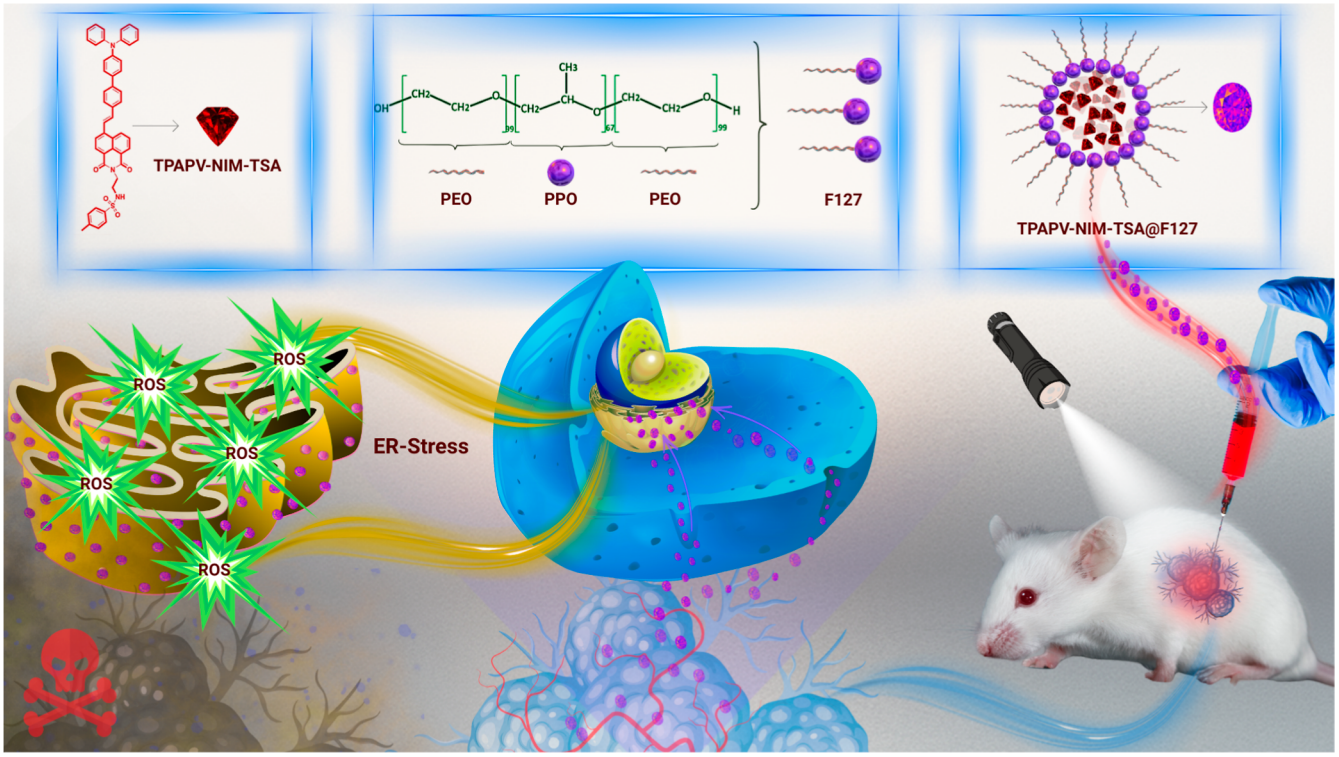

minimally affects normal cells and employs a targeted approach.[8] Photosensitizers (PSs) are the building blocks of this method, triggering the generation of reactive oxygen species (ROS) that, in turn, kill cancer cells when exposed to light or a specific wavelength laser.[9] By absorbing photon energy, ground-state PSs can be excited to the singlet state when exposed to light of a particular wavelength. Thereafter, they relax to the lowest excited singlet state (S1) via nonradiative internal conversion and, finally, reach the lowest triplet state (T1) via intersystem crossing (ISC), generating ROS.[10] To achieve optimal functionality, PSs must possess specific properties, including selective tumor-site accumulation, efficient ROS generation, effective light absorption, and negligible dark toxicity.[11,12]

Under physiological conditions, commonly used PSs, such as porphyrins and phthalocyanine derivatives, aggregate via $\pi-\pi$ stacking due to their large, planar, conjugated aromatic structures and poor water solubility, resulting in reduced fluorescence intensity or even fluorescence quenching and thereby affecting their ROS-generating ability. This phenomenon is known as the aggregation-caused quenching (ACQ) effect.[13−16] To address these challenges, a new phenomenon called aggregation-induced emission (AIE) was coined in 2001,[17] offering an effective strategy to overcome ACQ. AIE has gained popularity due to its adaptable optical properties, high ROS-generating capacity in aggregated states, strong fluorescence in both aggregated and solid states, and robust resistance to photobleaching.[18] Since its introduction, AIE has driven significant advances in sensing, imaging, and therapeutics. PSs with AIE features are promising candidates, as they exhibit high signal-to-noise ratios and high ROS generation yields, particularly in their aggregated states. In addition, the chemical structures of fluorophores with AIE characteristics can be easily tuned to target a desired cellular organelle, offering enticing opportunities to enhance the efficacy of PDT.[19,20] In cellular environments, PSs generate short-lived ROS that typically last for approximately 200 ns, and the ROS diffusion distance is restricted to 0.01−0.1 μm during this brief period, which is substantially smaller than the size of human cells (10−100 μm).[12,21,22] Therefore, for PDT to be effective, precise spatiotemporal control of ROS generation, ideally at defined subcellular organelles, is required. This can reduce the needed PS dose, minimize off-target damage, and improve therapeutic outcomes, making targeted PDT a promising strategy for precise cancer-cell ablation.[23−25]

The endoplasmic reticulum (ER), a vital organelle within a cell, performs multiple roles, including sensing, signal transduction, biosynthesis, and post-translational modification, and plays a significant role in maintaining cellular homeostasis.[26,27] Damage to the ER caused by a PS leads to the accumulation of misfolded proteins, disrupting ER homeostasis and inducing ER stress.[26] In response to stress, the ER initiates a cascade of signaling pathways collectively known as the unfolded protein response (UPR). Protein kinase RNA-like ER kinase (PERK), inositol-requiring enzyme 1 (IRE1), and activating transcription factor 6 (ATF6) are three branches of the UPR that encompass signaling in the ER, which primarily serve to increase cell viability, however, in the presence of severe oxidative stress, it is impossible to reestablish ER equilibrium, leading to the cell death.[28,29] Thus, targeting the ER is a promising approach for developing new-generation PSs that enhance the efficacy of phototherapy by disrupting ER homeostasis and promoting cancer cell death.[30,31]

The ability of the toluenesulfonamide (TSA) group to transport target molecules to the ER has also been well established in the literature.[32−36] Motivated by the effective-

https://doi.org/10.1021/acsami.5c25184
ACS Appl. Mater. Interfaces 2026, 18, 13516−13528

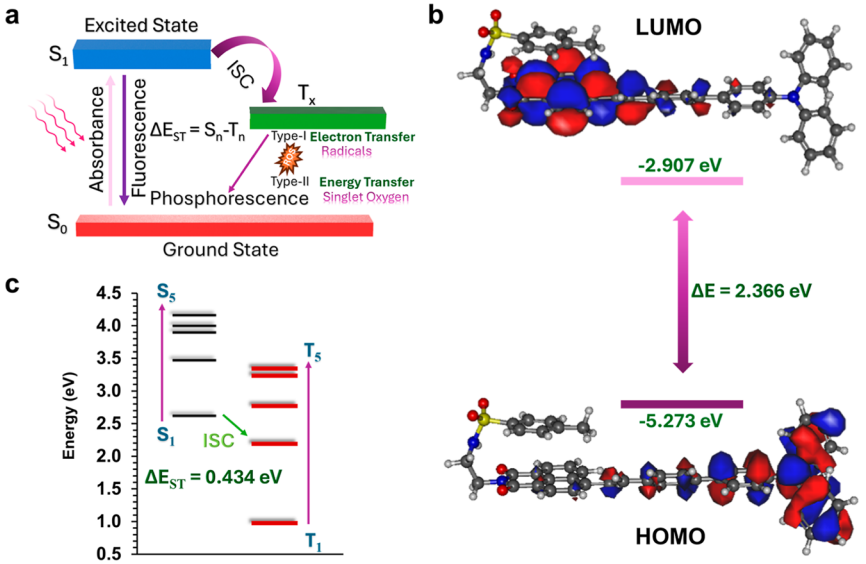

Figure 1. (a) Schematic illustration of the ROS generation via type I and type II pathways. (b) Pictorial representations of HOMO and LUMO energy levels of TPAPV-NIM-TSA. (c) Singlet and triplet energy levels of TPAPV-NIM-TSA calculated with TDDFT using ground-state geometry and CAM-B3LYP/6-31G* level of theory.

ness of PDT in antitumor applications, we present the synthesis and application of a novel naphthalimide-based donor−π−acceptor (D−π−A) type NIR−emitting PS, TPAPV-NIM-TSA. To improve aqueous dispersibility and cellular interaction, TPAPV-NIM-TSA was encapsulated in a Pluronic F127 nanocarrier to form TPAPV-NIM-TSA@F127, enabling ER−targeted anticancer therapy (Scheme 1). Although the naphthalimide core has been extensively explored for the synthesis of chemo- and biosensors,[37−39] it has been rarely investigated for photosensitizing applications, with only a few studies reported to date.[40−44] Here, we report, for the first time, a novel naphthalimide-based ER-targeted molecule, featuring electron donor−acceptor moieties separated by a π-bridge to induce extended π-conjugation, thereby endowing the molecule with high ROS generation ability and NIR-emission properties. TPAPV-NIM-TSA exhibits broad absorption in the visible region and can be readily activated by conventional white light to generate ROS, which, in turn, effectively induces the photodynamic destruction of cancer cells both in vitro and in vivo.

2. RESULTS AND DISCUSSION

2.1. Molecular Design and Theoretical Calculations of TPAPV-NIM-TSA

TPAPV-NIM-TSA is a donor−acceptor type molecule, and it was synthesized by a Heck cross-coupling reaction (Scheme S1). Organic molecules with strong donor−acceptor characteristics are ideal candidates for PDT, as this strategy can effectively separate the highest occupied molecular orbital (HOMO) from the lowest unoccupied molecular orbital (LUMO), thereby significantly reducing the energy gap between the singlet and triplet states and facilitating ISC to generate ROS.[45] To synthesize TPAPV-NIM-TSA, the naphthalimide skeleton was chosen as an acceptor moiety, and it was decorated with triphenyl amine (TPA) as a donor substituent, which can also help in the AIE phenomenon, owing to its twisted geometry to resist π−π stacking. A π-bridge was introduced between the donor and acceptor units to endow TPAPV-NIM-TSA with longer wavelength absorption and emission. The molecule was further functionalized with a TSA moiety to facilitate ER targeting. The sulfonamide group (−SO_2NH−) can engage in hydrogen-bonding interactions with ER-associated proteins and lipids, while the methylphenyl group (aromatic tolyl ring) promotes hydrophobic interactions with the ER membrane, together contributing to ER localization.[46] So, the synergistic combination of these polar and nonpolar units creates the amphiphilic balance, facilitating the PS to anchor at the ER membrane interface.[47] Thus, incorporating the TSA unit into a PS has the advantage of directing it to the ER and providing an ideal route for effective PDT of cancer cells under white light irradiation.

The underlying photodynamic ROS-generation process, involving both type I (radical-mediated) and type II ($^1O_2$-mediated) pathways upon light irradiation, is schematically illustrated in Figure 1a. To validate the design strategy of TPAPV-NIM-TSA, density functional theory (DFT) and time-dependent density functional theory (TDDFT) studies were conducted at the CAM-B3LYP/6-31G* level of theory (see Supporting Information for details), revealing that the electron cloud of the HOMO is predominantly localized on the donor moiety (triphenylamine). In contrast, the LUMO are associated with the naphthalimide acceptor unit of TPAPV-NIM-TSA (Figure 1b). The HOMO and LUMO energies were determined to be −5.273 eV and −2.907 eV, respectively, resulting in a HOMO−LUMO energy band gap (ΔE_{hl}) of 2.366 eV, indicating a typical donor−acceptor structure for TPAPV-NIM-TSA, which helps in reducing the energy gap (ΔE_{ST}) between the singlet and triplet excited states, thereby facilitating the ISC to generate ROS under light irradiation. The energies of the singlet and triplet states were calculated by TDDFT, and the ΔE_{ST} value for TPAPV-NIM-TSA was found to be 0.434 eV (Figure 1c and Table S1), which is small enough to facilitate the $S_1 \rightarrow T_2$ transitions with higher ISC rates to generate ROS under light illumination.

2.2. Nanoparticle Preparation and Characterization

TPAPV-NIM-TSA@F127 was prepared as reported in the literature.[48] Briefly, TPAPV-NIM-TSA (1 mg) and Pluronic

https://doi.org/10.1021/acsami.5c25184
ACS Appl. Mater. Interfaces 2026, 18, 13516−13528

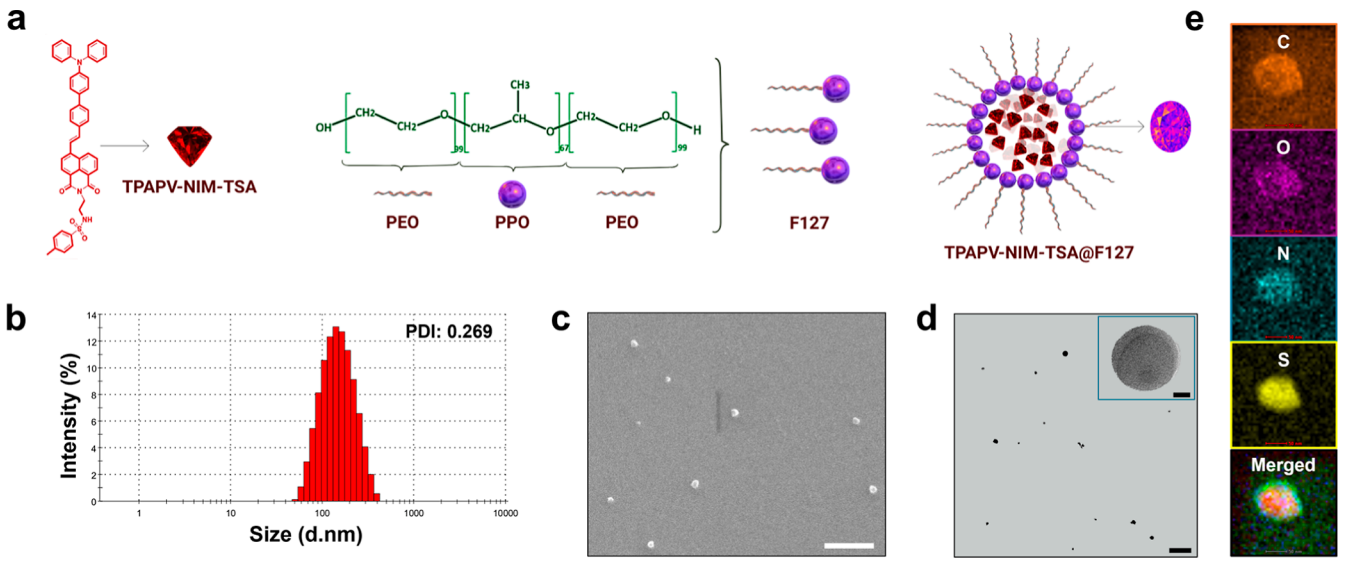

Figure 2. (a) Schematic illustration of the synthesis of TPAPV-NIM-TSA@F127. (b) DLS results of TPAPV-NIM-TSA@F127. (c) SEM image of TPAPV-NIM-TSA@F127. Scale bar: 300 nm. (d) TEM image of TPAPV-NIM-TSA@F127. Scale bar: 500 nm. (e) TEM−EDX elemental mapping images of TPAPV-NIM-TSA@F127 nanoparticles, showing the spatial distribution of C, N, O, and S elements.

F127 (19 mg) were separately dissolved in 1 mL of chloroform at room temperature. Then, the two solutions were mixed at a 1:1 volume ratio, followed by evaporation of chloroform under a nitrogen stream to obtain a mixture with a 1:19 ratio of TPAPV-NIM-TSA to Pluronic F127 (Figure 2a). The sample was dried in a vacuum dryer at 50 °C for 12 h, and the resulting nanoparticles were characterized by dynamic light scattering (DLS), scanning electron microscopy (SEM), and transmission electron microscopy (TEM). The hydrodynamic sizes of the nanoparticles were 159.50 nm, with a PDI of 0.269 (Figure 2b). The surface morphologies of the nanoaggregates were examined by SEM and TEM, revealing uniform spherical nanoparticles with an average size of 86.2 nm (Figure 2c,d). To further confirm the successful encapsulation and compositional homogeneity of the nanoparticles, TEM−EDX elemental mapping analysis was performed. The characteristic elements C, N, O, and S are uniformly distributed throughout the nanoparticle structure, indicating the effective incorporation of TPAPV-NIM-TSA within the Pluronic F127 matrix without phase separation (Figure 2e). The zeta potential of the synthesized nanoparticles was also measured using a zeta sizer, and the results are presented in Figure S1, which shows that TPAPV-NIM-TSA exhibits a zeta potential of −10.5 mV.

2.3. Photophysical Properties of TPAPV-NIM-TSA

UV−visible and fluorescence spectroscopic techniques were employed to investigate the photophysical properties of TPAPV-NIM-TSA in chloroform, and the results are illustrated in Figure 3. The maximum absorption of TPAPV-NIM-TSA was recorded at 437 nm (Figure 3a), while the maximum emission was recorded at 656 nm (Figure 3b), with a Stokes shift of 219 nm, which is large enough to help TPAPV-NIM-TSA to avoid self-quenching in the aggregated state. Owing to the presence of the TPA moiety, TPAPV-NIM-TSA was also expected to exhibit AIE behavior. To verify our prediction, tetrahydrofuran (THF)−water mixtures were used. In pure THF, TPAPV-NIM-TSA exhibited weak red fluorescence, but upon addition of water, fluorescence quenching was observed at 10% water content. With increasing water content, fluorescence was observed above 60% water content (Figure 3c,d), indicating that TPAPV-NIM-TSA exhibits an AIE phenomenon. Based on the above results, we conclude that TPAPV-NIM-TSA is a typical AIEgen and can be used in the PDT of cancer cells, as in the aggregated state, AIEgens block nonradiative pathways, resulting in a high quantum yield and stabilization of the triplet excited state, thereby boosting ROS generation.[49]

2.4. ROS and Singlet Oxygen Generation

The potential of TPAPV-NIM-TSA to generate ROS was evaluated using anthracenediyl-bis(methylene)-dimalonic acid (ABDA), a commercial $^1O_2$ sensor/indicator. Because TPAPV-NIM-TSA exhibits a strong absorbance in the visible region, the easily accessible and safe white light was used to evaluate the efficacy of TPAPV-NIM-TSA for generation in an aqueous medium using 75 μM ABDA and 10 μM TPAPV-NIM-TSA. Prior to the experiment, the molar absorption coefficient of TPAPV-NIM-TSA was measured in dimethyl sulfoxide (DMSO) at the absorption maximum; the results are presented in Figure S2, which shows a molar absorption coefficient of 41,490 M^{-1} cm^{-1}. The photostability of ABDA (75 μM) was also evaluated under white light irradiation, and after 120 s of exposure, no ABDA breakdown was observed (Figure 3e). Next, we irradiated ABDA (75 μM) in the presence of 10 μM TPAPV-NIM-TSA under white light (40 mW/cm^2) for 0−120 s. 75% of the ABDA was consumed within 120 s of white light irradiation, supporting that TPAPV-NIM-TSA can generate ROS under light illumination (Figure 3f). The singlet oxygen-generating ability of TPAPV-NIM-TSA was also evaluated by comparing it with the commercial PSs rose bengal (RB) and chlorin e6 (Ce6). Prior to the experiment, the molar absorption coefficients of RB and Ce6 were measured in DMSO at their respective absorption maxima, yielding molar absorption coefficients of 33,250 M^{-1} cm^{-1} and 43,200 M^{-1} cm^{-1}, respectively (Figures S3 and S4). For ROS generation comparison, the commercial PSs, RB and Ce6, were used under the same conditions as those for TPAPV-NIM-TSA, and it was found that Ce6 consumed 21% ABDA (Figure S5) and RB consumed up to 40% ABDA in 120 s of light irradiation (Figure S6). The comparison of ABDA

https://doi.org/10.1021/acsami.5c25184
ACS Appl. Mater. Interfaces 2026, 18, 13516−13528

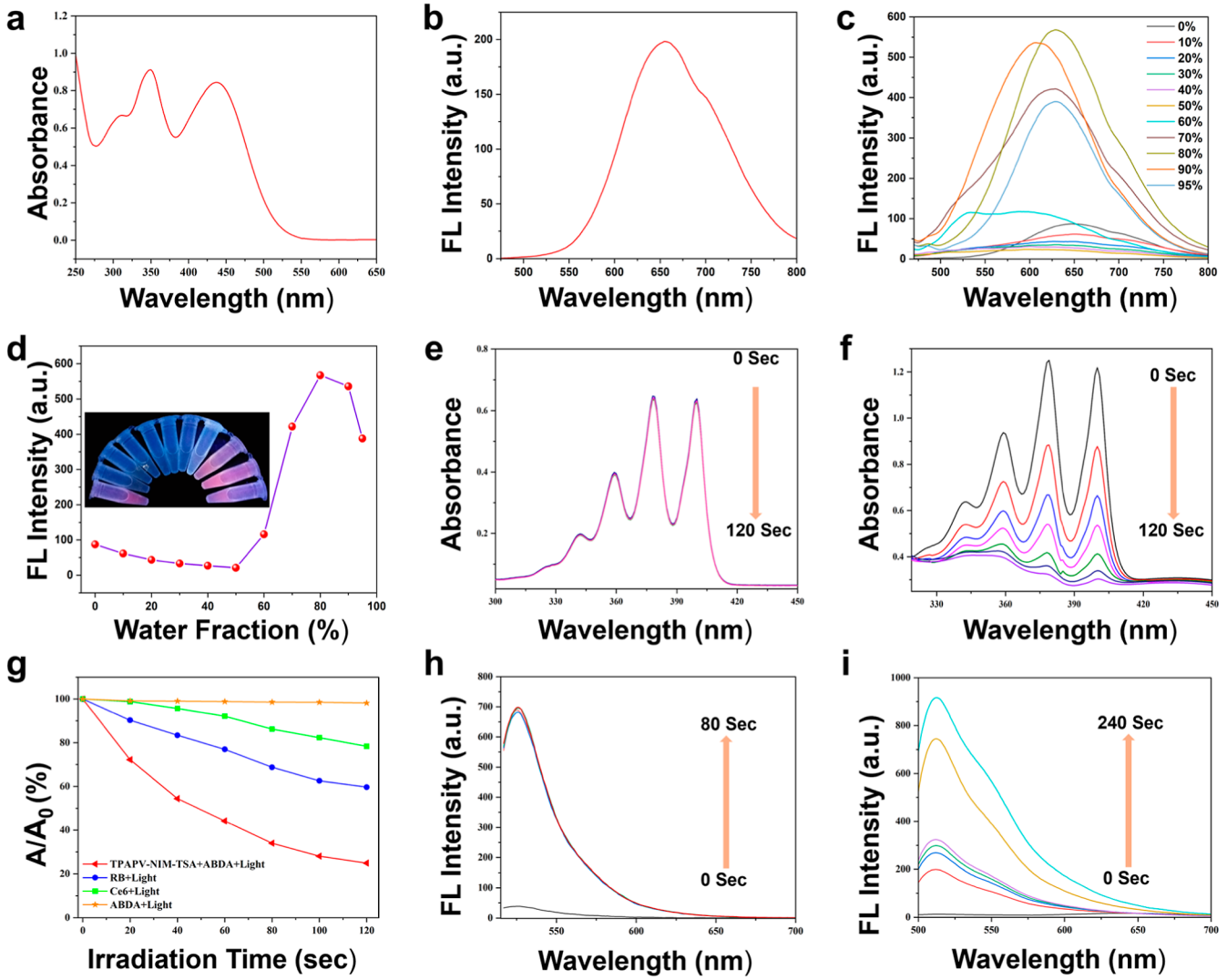

Figure 3. (a) Absorption spectrum of TPAPV-NIM-TSA in chloroform. (b) Fluorescence emission spectrum of TPAPV-NIM-TSA in chloroform. (c) Fluorescence emission spectra of TPAPV-NIM-TSA in THF−water mixtures with different water fractions based on volume. (d) Plot of the changes in the fluorescence intensities of TPAPV-NIM-TSA with varying fractions of water. (e) Absorption spectra of ABDA (75 μM) under white light irradiation. (f) Absorption spectra of ABDA in the presence of TPAPV-NIM-TSA (10 μM) under white light irradiation. (g) Decomposition rates of ABDA in the presence of different PSs (TPAPV-NIM-TSA, Ce6, and RB), where A/A_0 represents absorption of ABDA at 400 nm. (h) Fluorescence emission spectra of HPFP (2.5 μM) in the presence of TPAPV-NIM-TSA (2.5 μM) under white light irradiation. (i) Fluorescence emission spectra of DHR-123 (2.5 μM) in the presence of TPAPV-NIM-TSA (2.5 μM) under white light irradiation.

decompositions by TPAPV-NIM-TSA, Ce6, and RB is shown in Figure 3g. These findings demonstrate that TPAPV-NIM-TSA exhibits greater ROS-generating capacity under white light irradiation than the commercially available PSs.

2.5. Hydroxyl Radical (OH•) and Superoxide Anion ($O_2^{\bullet-}$) Detection

The capability of TPAPV-NIM-TSA to generate OH• was assessed utilizing hydroxyphenyl fluorescein (HPF) as a hydroxyl radical sensor. Stock solutions of HPF (1 mM) and TPAPV-NIM-TSA (1 mM) in DMSO were diluted to 2.5 μM in H_2O to prepare working solutions. After exposure to white light (~40 mW/cm^2), HPF fluorescence was observed at 500−620 nm at various time points, with excitation at 490 nm. The OH•-generating ability of TPAPV-NIM-TSA was assessed by measuring fluorescence at 515 nm. The fluorescence intensity increased periodically with increasing irradiation time, indicating that TPAPV-NIM-TSA can generate OH• (Figure 3h). Similarly, the generation of superoxide anion ($O_2^{\bullet-}$) was also investigated via DHR-123 in an aqueous medium from 0 to 80 s under the same conditions as those for OH• detection, and the changes in fluorescence intensity were recorded at 526 nm. With increasing irradiation time, the fluorescence intensity at 526 nm also increased, strongly supporting the generation of superoxide anions by TPAPV-NIM-TSA (Figure 3i).

2.6. Cytotoxicity and Confocal Study

Cytotoxicity is a crucial criterion for assessing the biosafety of a drug intended for biomedical research; therefore, we first assessed the cytotoxicity of TPAPV-NIM-TSA@F127 against HUVECs and MDA-MB-231 cells. To evaluate dark cytotoxicity, HUVECs and MDA-MB-231 cells were incubated with TPAPV-NIM-TSA@F127 at varying concentrations (0−50 μM) for 24 h in the dark. Subsequently, cell viability was evaluated using the conventional MTT assay, and the results presented in Figures S7 and S8 indicate that TPAPV-NIM-TSA@F127 is biocompatible. Next, we assessed the cellular interactions of TPAPV-NIM-TSA@F127 using confocal laser

https://doi.org/10.1021/acsami.5c25184
ACS Appl. Mater. Interfaces 2026, 18, 13516−13528

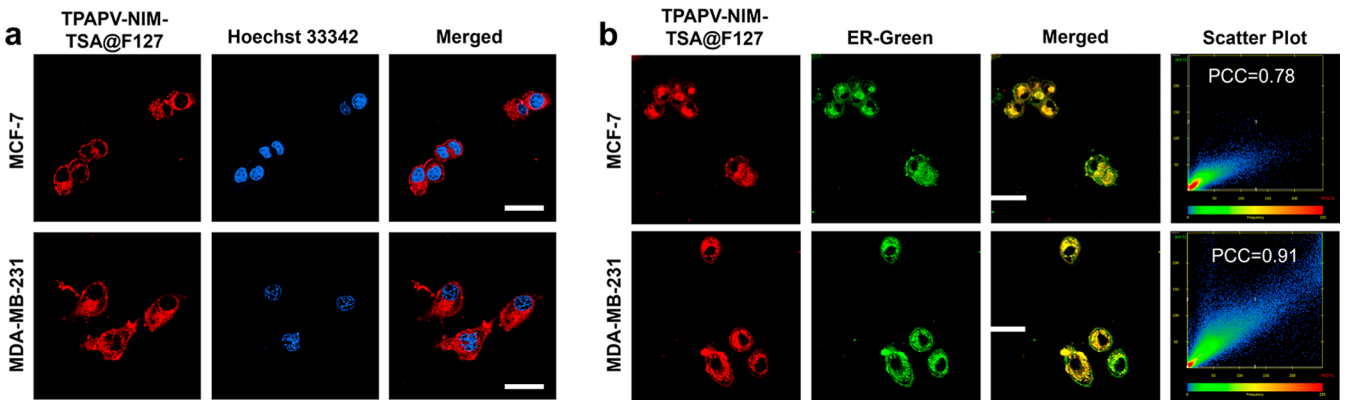

Figure 4. (a) Confocal fluorescence images of MCF-7 and MDA-MB-231 cells incubated with TPAPV-NIM-TSA@F127 (10 μM) and Hoechst 33342 (2 μM). (b) Confocal fluorescence images of MCF-7 and MDA-MB-231 cancer cells costained with TPAPV-NIM-TSA@F127 (10 μM) and ER-Green (3 μM). TPAPV-NIM-TSA@F127 was excited with a 488 nm laser, with emission collected between 610 and 700 nm. Hoechst 33342 was excited with a 405 nm laser, and emission was collected between 400 and 515 nm. ER-Green was excited with 488 nm, with emission collected between 490 and 560 nm. Scale bar: 10 μm.

scanning microscopy, a technique that is ideal for observing cellular and subcellular structures without causing significant cell damage. To observe the subcellular distribution of TPAPV-NIM-TSA@F127, MCF-7 and MDA-MB-231 cells were separately incubated with TPAPV-NIM-TSA@F127 (10 μM) and Hoechst 33342 (2 μM), followed by observation under a confocal laser scanning microscope. The red fluorescence signals are emitted from the cytoplasm, indicating a good, uniform subcellular distribution of TPAPV-NIM-TSA@F127 within the cells (Figure 4a). To confirm the subcellular distribution of TPAPV-NIM-TSA@F127, it was coincubated with the commercial ER dye (ER-Green) in MCF-7 breast cancer cells for 6 h and observed under a confocal laser scanning microscope. The red fluorescent signals from TPAPV-NIM-TSA@F127 overlapped well with the green signals from ER-Green, with a Pearson's correlation coefficient (PCC) of 0.78, confirming the aggregation of TPAPV-NIM-TSA@F127 in the ER. To further validate that TPAPV-NIM-TSA@F127 is an ER-specific fluorophore, it was coincubated with ER-Green in MDA-MB-231 cancer cells for 6 h and then observed under a confocal laser scanning microscope. The red signals from TPAPV-NIM-TSA@F127 overlapped well with the green signals from ER-Green, with a Pearson's correlation coefficient (PCC) of 0.91, further confirming the high affinity of TPAPV-NIM-TSA@F127 for the ER (Figure 4b).

2.7. In Vitro Photodynamic Therapy of Cancer Cells

Encouraged by the efficient ROS generation and favorable cellular interactions, further research was conducted to investigate the potential of the molecule for breast cancer treatment through PDT. The potential of TPAPV-NIM-TSA@F127 to generate ROS within cells was evaluated using 2′,7′-dichlorofluorescein diacetate (DCFH-DA), a commercially available ROS sensor. In a cellular environment, DCFH-DA is deacetylated by the intracellular esterase enzyme to non-fluorescent DCFH; upon light irradiation in the presence of a PS, it is oxidized to DCF with intense green fluorescence. MCF-7 breast cancer cells were incubated with 10 μM of TPAPV-NIM-TSA@F127 for 6 h in a glass-bottomed confocal dish to assess the intracellular ROS generation ability of TPAPV-NIM-TSA@F127. Thereafter, the cells were rinsed with PBS, treated with DCFH-DA (10 μM), and incubated for an additional 30 min. Next, the cells were rinsed twice with PBS and subsequently exposed to white light (~40 mW/cm^2) for 15 min; after that, they were examined using a confocal microscope. An intense green fluorescence can be observed in the light group (Figure 5a), attributed to the oxidation of DCFH by ROS generated by TPAPV-NIM-TSA@F127. The same procedure was used for the control group, in which the cells were incubated with DCFH-DA (10 μM) and Hoechst 33342. In contrast, in the control group, the MCF-7 cells cultured with DCFH-DA and Hoechst 33342 did not show any green fluorescence upon exposure to light (Figure 5a), demonstrating that TPAPV-NIM-TSA@F127 can generate intracellular ROS, which is essential for the PDT of cancer cells. In addition, a control group containing TPAPV-NIM-TSA@F127 and DCFHDA in MCF-7 cells under dark conditions was also investigated; no green fluorescence signals were observed, further confirming TPAPV-NIM-TSA@F127's ability to generate ROS under light illumination (Figure S9). Furthermore, we investigated the effects of ROS inhibitors (vitamin C and glutathione) on ROS generation under light irradiation, as can be seen from Figure S9, that in the presence of vitamin C and glutathione, no green fluorescence signals were observed, further confirming that our synthesized PS can generate ROS under white light irradiation.

The outstanding intracellular ROS generation by TPAPV-NIM-TSA@F127 encouraged us to investigate it further for in vitro photodynamic ablation of cancer cells. To evaluate the photodynamic ability of TPAPV-NIM-TSA@F127, two different cancer cells, MCF-7 and MDA-MB-231, were separately incubated with TPAPV-NIM-TSA@F127 at concentrations ranging from 0 to 10 μM for 6 h. Thereafter, the cells were exposed to white light at approximately 40 mW/cm^2 for 25 min, followed by an additional 12 h of incubation. Afterward, cell viability was evaluated using the standard MTT assay. Cell viability decreased with increasing TPAPV-NIM-TSA@F127 concentration, indicating strong phototoxicity under white light irradiation (Figure 5b). Next, we used the annexin V-FITC/PI kit to quantitatively monitor cellular apoptosis induced by TPAPV-NIM-TSA@F127 by flow cytometry, an ideal technique for deeper insight into the photodynamic ablation of cancer cells under light irradiation. To perform flow cytometry analysis, 1 × 10^6 MCF-7 cells were cultured with TPAPV-NIM-TSA@F127 (10 μM) for 6 h in a glass-bottom confocal dish, followed by treatment with annexin V-FITC/PI

https://doi.org/10.1021/acsami.5c25184
ACS Appl. Mater. Interfaces 2026, 18, 13516−13528

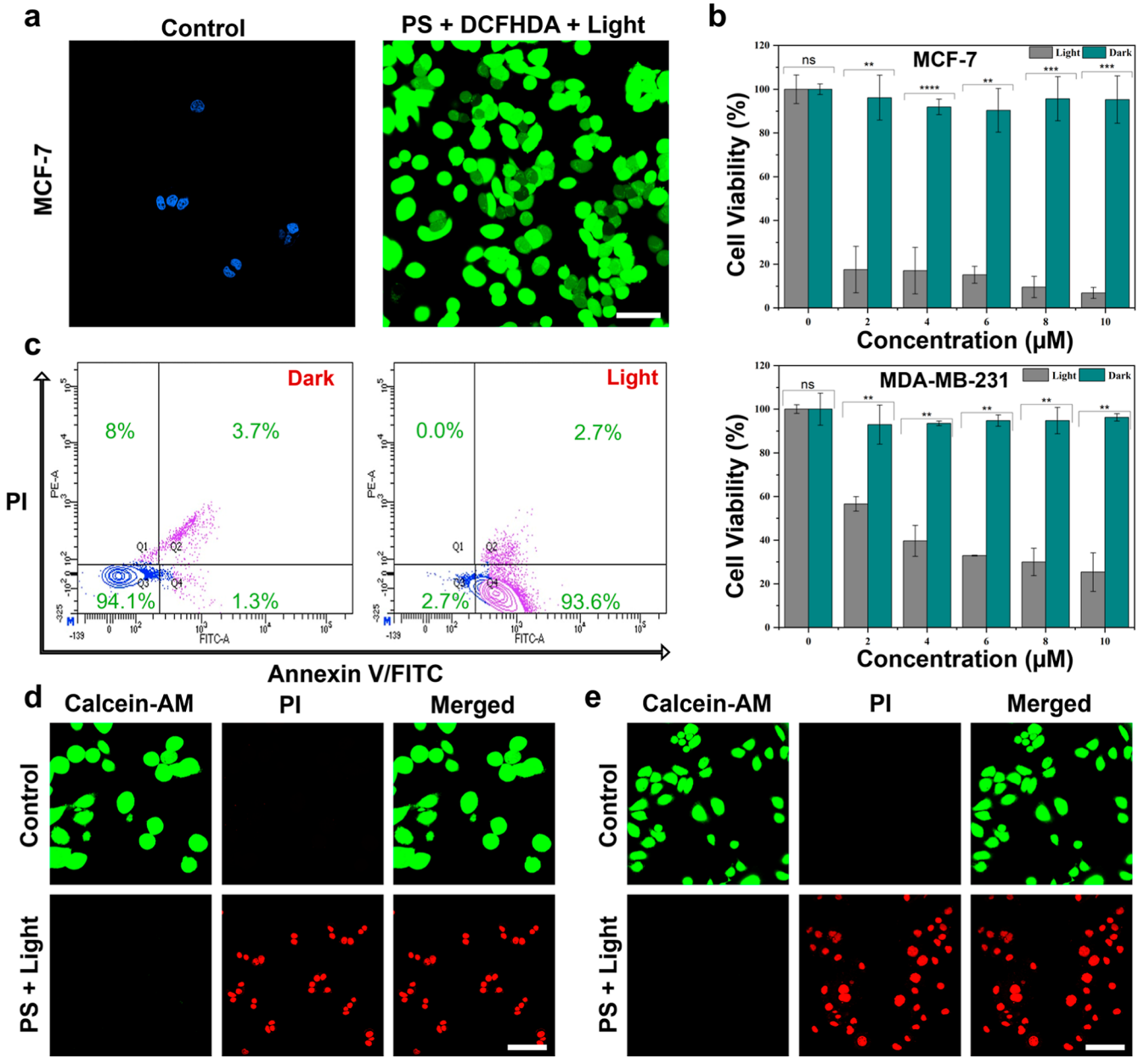

Figure 5. (a) Detection of intracellular ROS via DCFH-DA (10 μM) in MCF-7 breast cancer cells. Light intensity ~ 40 mW/cm^2. DCF was excited with a 488 nm laser, and the emission was collected between 490 and 560 nm. Scale bar: 20 μm. (b) Cell viability of MCF-7 and MDA-MB-231 cancer cells incubated with different concentrations of TPAPV-NIM-TSA@F127 (0−10 μM) in the dark and under white light irradiation for 25 min (~40 mW/cm^2) (mean ± SD, $n = 6$), *$p < 0.05$, **$p < 0.01$, ***$p < 0.001$, ****$p < 0.0001$, and ns (not significant) as determined by the Student's t-test. (c) Apoptosis tracking in MCF-7 cells: dark (MCF-7 cells only treated with annexin V-FITC/PI under dark) and light (MCF-7 cells treated with TPAPV-NIM-TSA@F127 and annexin V-FITC/PI under light). Light intensity ~ 40 mW/cm^2. (d) Live−dead cell assay in MCF-7 cancer cells treated with TPAPV-NIM-TSA@F127 (10 μM). (e) Live−dead cell assay in MDA-MB-231 cancer cells treated with TPAPV-NIM-TSA@F127 (10 μM): live cells were labeled by calcein-AM with green fluorescence, and PI labeled dead cells with red fluorescence. Calcein-AM was excited at 488 nm, and the emission was collected between 450 and 555 nm. The PI was excited with a 561 nm laser, and the emission was collected between 450 and 700 nm. Scale bar: 20 μm.

according to the manufacturer's protocol. Thereafter, the cells were analyzed using flow cytometry as soon as possible. TPAPV-NIM-TSA@F127 induced apoptosis effectively in MCF-7 cancer cells, further confirming the efficacy of TPAPV-NIM-TSA@F127 for PDT of cancer cells (Figure 5c).

2.8. Live−Dead Cell Staining

To further assess the efficacy of TPAPV-NIM-TSA@F127 in PDT, a live−dead cell staining experiment was conducted utilizing a calcein-AM (calcein acetoxymethyl ester) and PI (propidium iodide) kit. Calcein-AM is nonfluorescent, but after cellular uptake, the cellular esterase enzyme breaks it down into green fluorescent calcein, which is often used to distinguish live cells from dead cells. PI, on the other hand, penetrates to the nucleus of dead cells and emits bright red fluorescence. To perform a live−dead cell assay, MCF-7 and MDA-MB-231 cancer cells were incubated separately with TPAPV-NIM-TSA@F127 (10 μM) for 6 h in a glass-bottom confocal dish. After that, the light groups were exposed to white light for 14 min; thereafter, they were treated with

https://doi.org/10.1021/acsami.5c25184
ACS Appl. Mater. Interfaces 2026, 18, 13516−13528

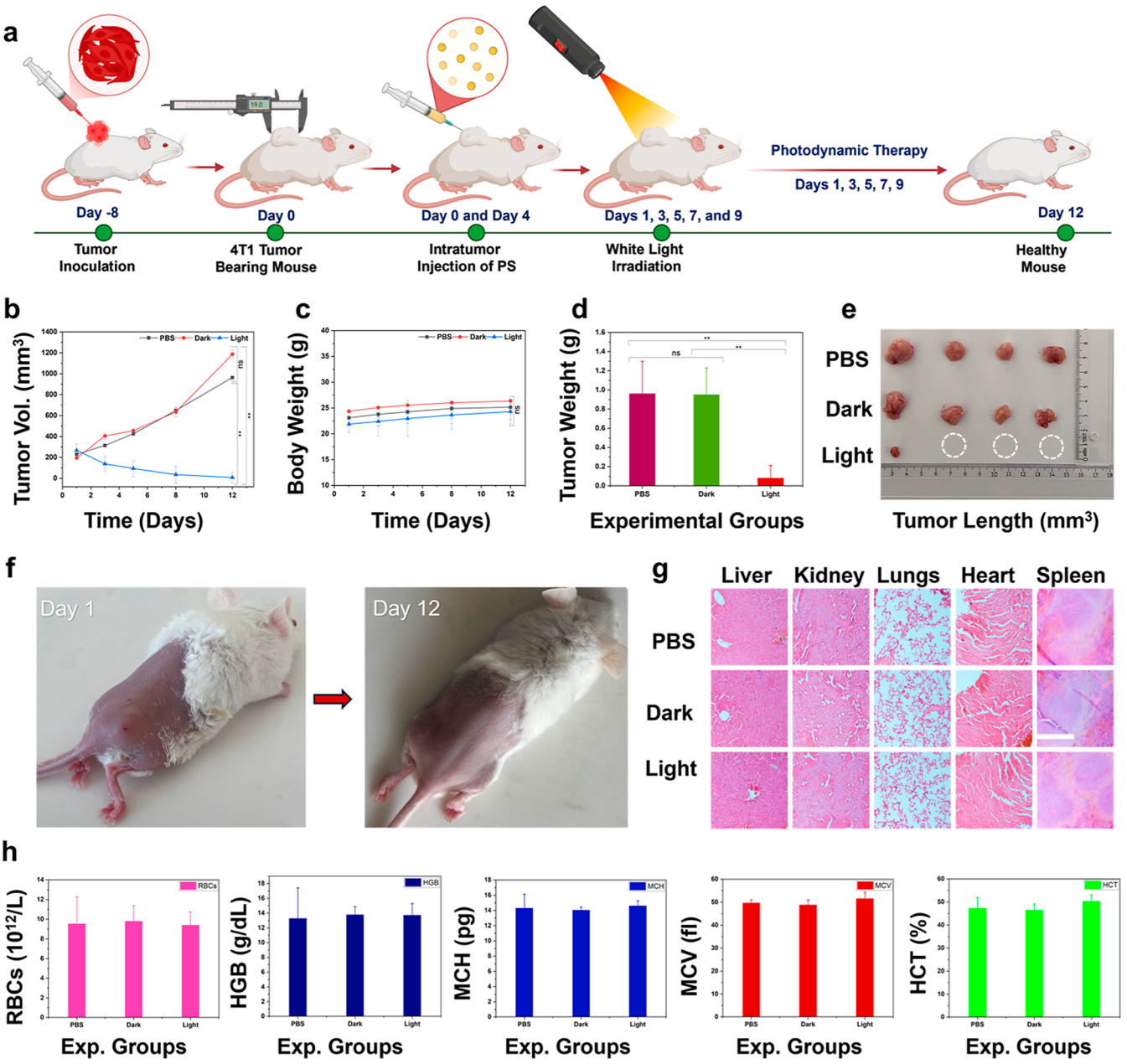

Figure 6. (a) Experimental design and schedule for the antitumor PDT of 4T1 tumor-bearing BALB/c mice. (b) Changes in the tumor volume of different treatment groups during the antitumor PDT experiment. (c) Changes in the body weights of mice of different treatment groups during the antitumor PDT experiment. (d) Average weight of the tumors excised from the different treatment groups at the end of the PDT experiment. (e) Photograph of the tumors excised from the different treatment groups at the end of the PDT experiment. (f) Photographs of the mouse bearing the 4T1 tumor before and after the PDT. (g) H&E staining images of vital tissues (liver, kidney, lungs, heart, and spleen) after 12 days of various treatments of the 4T1 tumor-bearing BALB/c mice. Scale bar: 50 μm. (h) Hematological parameters of the blood samples collected from mice of the different treatment groups after 12 days of the PDT experiment. Data are represented as (mean ± SD, $n = 4$), statistical significance levels are indicated as $^{*}p < 0.05$, $^{**}p < 0.01$, $^{***}p < 0.001$, $^{****}p < 0.0001$, and ns (not significant). Student's t-test was used.

calcein-AM (2 μM) and PI (8 μM) for 15 min at 37 °C, and then the cells were washed twice with PBS, followed by examination under a confocal microscope as soon as possible. According to the confocal microscopy results, the control groups (dark groups) showed intense green fluorescence, indicating that TPAPV-NIM-TSA@F127 did not exhibit dark toxicity. In contrast, the light-treated groups exhibited bright red fluorescent signals (Figure 5d,e), indicating efficient photodynamic killing of cancer cells under light irradiation.

2.9. In Vivo Antitumor Therapy in 4T1 Tumor-Bearing Mice

Motivated by the strong ROS generation (in vitro and in vivo), low dark toxicity, effective cellular staining, negligible hemolysis, and the pronounced photodynamic killing of cancer cells, we further evaluated TPAPV-NIM-TSA@F127 for in vivo antitumor PDT in 4T1-tumor-bearing BALB/c mice. Five-week-old female BALB/c mice were purchased from the animal facility at Erciyes University and divided into three groups ($n = 4$): PBS, dark, and light. They were then infected with 4T1 tumor cells. All infected mice were regularly

https://doi.org/10.1021/acsami.5c25184
ACS Appl. Mater. Interfaces 2026, 18, 13516−13528

monitored, and when tumor volumes reached 100 mm^3 (on day 7), they received different treatments (Figure 6a). The PBS group received 200 μL of PBS, the dark group received 200 μL of TPAPV-NIM-TSA@F127 solution in PBS (200 μM), and the light group received 200 μL of TPAPV-NIM-TSA@F127 solution in PBS (200 μM) via intratumoral injection. After 24 h, the PBS and light groups were irradiated with white light (~85 mW/cm^2) for 25 min, while the dark group did not receive light therapy. On day 5, the light and dark groups received an additional 200 μL of TPAPV-NIM-TSA@F127 solution in PBS (200 μM) via intratumoral injection. The mice's weight and tumor size were also measured every second day (Figure 6b,c), and the PDT progress was documented photographically until day 12 (Figure S10). The PDT treatment was repeated every second day for the PBS and light groups until day 9, and near-complete tumor eradication was achieved by day 12 (Figure 6d,e), demonstrating the strong antitumor efficacy of TPAPV-NIM-TSA@F127. Representative images further corroborate the treatment outcome: a clear tumor mass is visible on day 1 before irradiation, but after PDT the tumor region appears markedly regressed and is not visually apparent by day 12 (Figure 6f). On day 12, blood was collected from all groups, and all mice were sacrificed. The vital organs, including the liver, heart, spleen, lungs, and kidneys, were then collected for hematoxylin and eosin (H&E) staining. All organs were intact, and no damage was observed, indicating biocompatibility of TPAPV-NIM-TSA@F127 (Figure 6g). Similarly, the basic blood parameters were within reference ranges, as determined by the hematological assay, further supporting the biosafety of TPAPV-NIM-TSA@F127 (Figure 6h). In addition, the hemolytic effect of TPAPV-NIM-TSA@F127 on red blood cells (RBCs) collected from a healthy mouse was also investigated. No hemolytic effect was observed even at a high concentration (200 μM) (Figure S11). Based on the above results, we can conclude that TPAPV-NIM-TSA@F127, with a high biosafety profile, not only selectively stains the ER but also effectively suppresses tumor growth and induces tumor regression, providing a novel platform for designing next-generation ER-based PSs for breast cancer PDT.

3. CONCLUSION

In this work, we designed, synthesized, and comprehensively evaluated a naphthalimide-based AIE PS, TPAPV-NIM-TSA, and its Pluronic F127-encapsulated nanoparticle formulation (TPAPV-NIM-TSA@F127) as an ER-targeted platform for photodynamic cancer therapy. The rational molecular architecture, which combined a donor−π−acceptor framework, extended π-conjugation, and a toluenesulfonamide-derived ER-targeting unit, enabled NIR fluorescence, AIE, and efficient photodynamic activity under low-intensity white light irradiation. Encapsulation in Pluronic F127 enhanced aqueous dispersibility, cellular uptake, and in vivo compatibility while maintaining the PS's intrinsic photophysical and organelle-targeting properties. This study demonstrated that precise subcellular targeting played a decisive role in amplifying photodynamic efficacy. Selective accumulation of TPAPV-NIM-TSA@F127 in the ER confined ROS generation to the ER, resulting in effective photodynamic cancer cell ablation while minimizing nonspecific oxidative damage to other cellular compartments. Notably, TPAPV-NIM-TSA@F127 activated both type I and type II ROS pathways under white light irradiation, thereby addressing limitations associated with conventional PSs that rely predominantly on oxygen-dependent mechanisms or require high-energy light sources. These findings highlighted the advantages of integrating AIE characteristics with organelle-specific targeting to achieve efficient ROS production in aggregated and biologically relevant environments. The therapeutic potential of this materials platform was further validated in 4T1 tumor-bearing BALB/c mice, where TPAPV-NIM-TSA@F127 produced significant tumor growth inhibition and near-complete tumor eradication upon white light irradiation, while exhibiting negligible systemic toxicity, minimal hemolysis, and preserved histological integrity of major organs. The combination of effective antitumor activity and a favorable biosafety profile underscore the translational relevance of this approach. Overall, this work establishes a versatile molecular and materials design strategy for ER-targeted AIE PSs that integrate imaging capabilities, dual ROS-generating pathways, and white light activation. The design principles and functional insights presented herein are expected to inform the development of next-generation organelle-specific phototherapeutic materials and to stimulate broader exploration of ER-centered strategies for precision cancer phototherapy.

4. EXPERIMENTAL SECTION

4.1. Materials and Instrumentation

Ethylenediamine, *p*-toluenesulfonyl chloride, sodium sulfate, 4-(diphenylamino)phenyl boronic acid, 4-bromostyrene, 4-bromo-1,8-naphthalic anhydride, tetrakis(triphenylphosphine) palladium(0) ($Pd(PPh_3)_4$), palladium(II) acetate, and sodium carbonate were purchased from Ambeed (USA). Triethylamine, iodomethane, potassium hexafluorophosphate, and Pluronic F127 were purchased from Sigma-Aldrich (USA). Calcein-AM/PI and annexin V-FITC/PI kits were purchased from Thermo Fisher Scientific. Hoechst 33342 and Endoplasmic Reticulum Green (ER-Green) were purchased from MedChemExpress (USA). Organic solvents were purchased from the local commercial suppliers and used as received without further purification. Nuclear magnetic resonance (NMR) spectroscopy (Bruker DRX-400 MHz spectrometer) was used to characterize the chemical structures of the synthesized molecules in $CDCl_3$ or DMSO-d_6 at room temperature. UV−vis and fluorescence spectra were recorded via a UV−vis spectrophotometer (PerkinElmer Lambda-25) and a spectrofluorophotometer (Cary Eclipse, Germany). Dynamic light scattering (DLS) was employed to determine the size of nanoaggregates using a Zetasizer (Malvern Nano ZS-90). The surface morphologies of the nanoaggregates were examined using a scanning electron microscope (SEM, ZEISS GEMINI-500). A confocal laser scanning microscope (ZEISS LSM-900, 63× oil immersion, confocal mode) was used to acquire confocal images. Cell apoptosis was tracked using flow cytometry (FACSAria III), and the data were analyzed with FlowJo version 10.0.7.

4.2. Synthesis Procedures

TPAPV-NIM-TSA and other precursor molecules were synthesized according to modified literature protocols and characterized by NMR and MS spectroscopy. The NMR and MS spectra are given in Figures S12−S19.

4.2.1. Synthesis of *p*-Toluenesulfonamide (*p*-TSA). 0.788 g (13.113 mmol) of ethylenediamine was dissolved in 7.0 mL of dichloromethane and stirred at room temperature for 5 min. Thereafter, it was treated with 0.5 g (2.623 mmol) of *p*-toluenesulfonyl chloride in 7.0 mL of dichloromethane and stirred at 40 °C for 1 h. The resulting product was extracted with brine, dried with sodium sulfate, and concentrated under vacuum to give a white solid 0.438 g (yield: 60.27%). ^1H NMR ($CDCl_3$, 400 MHz): δ/ppm = 2.43 (s, 3H), 2.79 (m, 2H), 2.96 (m, 2H), 7.31 (d, J = 8 Hz, 2H), 7.76 (d, J = 8 Hz, 2H).

https://doi.org/10.1021/acsami.5c25184
ACS Appl. Mater. Interfaces 2026, 18, 13516−13528

4.2.2. Synthesis of TSA-NIM. 0.3 g (1.083 mmol) of 4-bromo-1,8-naphthalic anhydride was dissolved in absolute ethanol (15 mL) and heated to reflux. This was followed by the injection of 0.237 g (1.191 mmol) of *p*-toluenesulfonamide in ethanol, and the resulting mixture was refluxed for a further 2 h. Thereafter, the reaction was stopped and cooled to room temperature. The resulting precipitate was collected by vacuum filtration, then washed with ethanol. The resulting product was dried at 50 °C under vacuum overnight to give 0.382 g of off-white solid (yield: 74.52%). ^{1}H NMR ($CDCl_3$, 400 MHz): δ/ppm = 2.23 (s, 3H), 3.10 (m, 2H), 4.09 (m, 2H), 7.18 (d, J = 8 Hz, 2H), 7.55 (d, J = 8 Hz, 2H), 7.76 (s, 1H), 7.99 (t, J = 8 Hz, 1H), 8.21 (d, J = 8 Hz, 1H), 8.28 (d, J = 8 Hz, 1H), 8.53 (m, 2H). HRMS (ESI): (m/z) calculated for $C_{21}H_{17}BrN_2O_4S$ $[M + H]^+$, 473.01652; found, 473.01834.

4.2.3. Synthesis of TPA-PV. It was synthesized via a Suzuki cross-coupling reaction between 4-(diphenylamino) phenyl boronic acid (TPA-B$(OH)_2$) and 4-bromostyrene. Briefly, 0.6 g (3.278 mmol) 4-bromostyrene, 1.043 g (3.606 mmol) TPA-B$(OH)_2$, 0.095 g Pd$(PPh_3)_4$ (0.082 mmol), and 1.042 g (9.833 mmol) sodium carbonate were added to a Schlenk flask. The flask was sealed and degassed multiple times. Subsequently, 21.0 mL of toluene, 6.0 mL of ethanol, and 3.0 mL of deionized water were injected, respectively. The mixture was purged with nitrogen gas and refluxed at 90 °C for 12 h under nitrogen. After successful completion of the reaction, as confirmed by thin-layer chromatography (TLC), the mixture was extracted with deionized water and brine, dried with anhydrous sodium sulfate, and concentrated under reduced pressure. The impure product was purified by silica gel column chromatography using a dichloromethane−*n*-hexane mixture (1:6) as the eluent to obtain 0.922 g of a white solid (yield: 80.95%). ^{1}H NMR ($CDCl_3$, 400 MHz): δ/ppm = 5.27 (d, J = 12 Hz, 1H), 5.80 (d, J = 20 Hz, 1H), 6.77 (m, 1H), 7.05 (t, J = 8 Hz, 2H), 7.16 (m, 6H), 7.29 (m, 4H), 7.49 (m, 4H), 7.56 (d, J = 8 Hz, 2H). ^{13}C NMR ($CDCl_3$, 100 MHz): δ/ppm = 113.60, 122.97, 123.85, 124.45, 126.67, 127.57, 129.29, 134.56, 136.11, 136.45, 140.02, 147.25, 147.65. HRMS (ESI): (m/z) calculated for $C_{26}H_{21}N$ $[M + H]^+$, 348.17467; found, 348.17681.

4.2.4. Synthesis of TPAPV-NIM-TSA. TPAPV-NIM-TSA was synthesized via the Heck cross-coupling reaction. 0.340 g (0.0.719 mmol) TSA-NIM, 0.2 g (0.575 mmol) TPA-PV, 0.013 g (0.0575 mmol) palladium(II) acetate, and 0.035 g (0.115 mmol) tri(*o*-tolyl) phosphine were taken in a Schlenk flask, and the flask was degassed multiple times. 15.0 mL of dry acetonitrile and 1.123 mL of triethylamine were injected, respectively. The mixture was purged with nitrogen and refluxed at 90 °C for 48 h under nitrogen. Thereafter, acetonitrile was removed under vacuum, and the resulting reaction mixture was taken up in dichloromethane (DCM), extracted with deionized water, washed with brine, dried over anhydrous sodium sulfate, filtered, and concentrated under reduced pressure. The resulting mixture was purified by silica gel column chromatography using a 5:1 mixture of tetrahydrofuran and methanol to obtain 0.134 g of a dark yellow solid (yield: 51.43%). ^{1}H NMR (DMSO-d_6, 400 MHz): δ/ppm = 2.24 (s, 3H), 3.12 (m, 2H), 4.12 (m, 2H), 7.08 (m, 8H), 7.19 (d, J = 8 Hz, 2H), 7.34 (t, J = 8 Hz, 4H), 7.59 (d, J = 8 Hz, 2H), 7.68 (t, J = 8 Hz, 3H), 7.74 (d, J = 8 Hz, 2H), 7.91 (m, 3H), 8.24 (t, J = 8 Hz, 2H), 8.45 (d, J = 8 Hz, 1H), 8.50 (d, J = 8 Hz, 1H), 9.01 (d, J = 8 Hz, 1H). ^{13}C NMR (DMSO-d_6, 100 MHz): δ/ppm = 21.34, 121.10, 123.59, 123.73, 123.82, 124.71, 126.80, 127.36, 127.92, 128.00, 128.59, 128.66, 129.44, 129.92, 130.09, 131.14, 133.60, 135.12, 135.69, 138.11, 140.11, 141.42, 142.86, 147.42, 163.64, 163.97. HRMS (ESI): (m/z) calculated for $C_{47}H_{37}N_3O_4S$ $[M]^+$, 739.25048; found, 739.24234.

4.3. Cell Culture

MCF-7 breast cancer cells were cultivated at 37 °C in a humid environment with 5% CO_2 in Roswell Park Memorial Institute (RPMI) 1640 cell culture media supplemented with 10% fetal bovine serum (FBS) and 1% penicillin−streptomycin. MDA-MB-231 and 4T1 cells were cultivated at 37 °C in a humid environment with 5% CO_2 in Dulbecco's modified Eagle's medium (DMEM) supplemented with 10% fetal bovine serum (FBS) and 1% penicillin−streptomycin.

4.4. Laser Scanning Confocal Fluorescence Imaging

To assess the imaging efficacy of TPAPV-NIM-TSA@F127, live cells were incubated with 10.0 μM/mL TPAPV-NIM-TSA@F127 at 37 °C for 6 h, followed by PBS washing. The cells were then stained with 2.0 μM/mL Hoechst 33342 and incubated for 5 min at 37 °C. After a 5 min incubation, the cells were washed with PBS and examined under a confocal microscope equipped with a 63× oil-immersion objective. The subcellular distribution of TPAPV-NIM-TSA@F127 was analyzed using the same methodology described above, in which cells were treated with TPAPV-NIM-TSA@F127 (10.0 μM/mL) for 6 h and ER-Green (3.0 μM/mL) for 30 min, then observed using a confocal laser scanning microscope equipped with a 63× oil-immersion objective.

4.5. Reactive Oxygen Species Detection

4.5.1. Singlet Oxygen Detection in Aqueous Medium. A standard commercial indicator for $^1O_2$ detection, ABDA, was used to assess the production of extracellular ROS in an aqueous medium. TPAPV-NIM-TSA (20 μM) and ABDA (150 μM) aqueous solutions were mixed in a 1:1 ratio to achieve the final working solution with concentrations of 10 μM and 75 μM for TPAPV-NIM-TSA and ABDA, respectively. The resulting mixture was exposed to white light (40 mW/cm^2) for 0−120 s, and the decomposition of ABDA at 400 nm was monitored using a UV−visible spectrophotometer. To evaluate the efficacy of our synthesized PS, we employed the commercial PSs rose bengal (10 μM) and chlorin e6 (10 μM) following the same protocol as for TPAPV-NIM-TSA and analyzed the decomposition of ABDA at 400 nm using a UV−visible spectrophotometer.

4.5.2. Hydroxyl Radical (OH$^\bullet$) Detection in Aqueous Medium. The OH$^\bullet$-generating capability of TPAPV-NIM-TSA was assessed by utilizing hydroxyphenyl fluorescein (HPF) as a hydroxyl radical sensor. Stock solutions of HPF (1 mM) and TPAPV-NIM-TSA (1 mM) in DMSO were diluted to 2.5 μM in H_2O to prepare working solutions. After exposure to white light (∼40 mW/cm^2), HPF fluorescence was observed at 515 nm at various time intervals.

4.5.3. Superoxide Anion ($O_2^{\bullet-}$) Detection in Aqueous Medium. The generation of superoxide anion ($O_2^{\bullet-}$) was investigated via DHR-123 in an aqueous medium. Stock solutions of DHR-123 (1 mM) and TPAPV-NIM-TSA (1 mM) in DMSO were diluted to 2.5 μM in H_2O to prepare working solutions. After exposure to white light (∼40 mW/cm^2) at various time intervals, the changes in fluorescence intensity were recorded at 526 nm.

4.5.4. Total ROS Detection in Cancer Cells. DCFH-DA, a standard commercial indicator for detecting intracellular ROS, was used to assess intracellular ROS generation. Following a 24 h incubation period in RPMI-1640 cell culture media, MCF-7 breast cancer cells were treated with TPAPV-NIM-TSA@F127 (10 μM) and incubated for an additional 6 h. Following a PBS wash, the cells were treated with 10 μM DCFH-DA, incubated for an additional 30 min, rinsed with PBS, exposed to white light (40 mW/cm^2) for 15 min, and examined under a confocal microscope as soon as possible.

4.6. Cytotoxicity Evaluation

4.6.1. Dark Toxicity. MDA-MB-231 and MCF-7 cancer cell lines were seeded at 5 × 10^3 cells per well in 96-well plates and incubated for 24 h. Afterward, the cells were treated with varying doses (0, 2, 4, 6, 8, and 10 μM/mL) of TPAPV-NIM-TSA@F127 and incubated for an additional 12 h. To assess the cytotoxicity of TPAPV-NIM-TSA@F127, the 3-(4,5-dimethyl-2-thiazolyl)-2,5-diphenyltetrazolium bromide (MTT) assay was performed by adding 10 μL of MTT solution in PBS (5 mg/mL) to each well to assess the cell viability, which was then incubated for 4 h at 37 °C. After discarding the culture medium, including the unreacted MTT, 150 μL of DMSO was added to each well to dissolve the resulting formazan crystals. The plate was then agitated for an additional 10 min, and cell viability was measured at 640/570 nm using a multimode microplate reader (Biotek, HTX S1 LFA, USA). Cell viability was calculated using the following formula.

https://doi.org/10.1021/acsami.5c25184
ACS Appl. Mater. Interfaces 2026, 18, 13516−13528

$$\text{Cell viability (\%)} = \frac{(OD_{Sample} - OD_{Blank})}{(OD_{Control} - OD_{Blank})} \times 100$$

4.6.2. Light Toxicity. The phototoxicity of TPAPV-NIM-TSA@F127 against MDA-MB-231 and MCF-7 cancer cells was assessed using the same methodology as for dark toxicity, except white light irradiation. Briefly, after a 6 h incubation with TPAPV-NIM-TSA@F127, the cells were exposed to white light (40 mW/cm^2) for 25 min, followed by a 12 h incubation. Then, the cells were subjected to MTT dye treatment and incubated for an additional 4 h, after which cell viability was assessed using the same approach as for dark toxicity.

4.7. Live–Dead Cell Staining

A glass-bottomed confocal dish was used to cultivate 50 × 10^3 cells of MCF-7 and MDA-MB-231 breast cancer cells for 24 h. After that, the cells were incubated with 10 μM TPAPV-NIM-TSA@F127 for 6 h, then washed with PBS and subjected to white light illumination (40 mW/cm^2) for 15 min. The cells were subsequently stained with 8.0 μM propidium iodide and 2.0 μM calcein-AM, then incubated for 15 min at 37 °C. Subsequently, the cells were carefully rinsed with PBS and examined under a confocal microscope. For comparison, MCF-7 and MDA-MB-231 cells (50 × 10^3 cells) were cultivated in separate confocal dishes as control groups, illuminated under white light (40 mW/cm^2) for 15 min, followed by calcein-AM/PI treatment for 15 min, and then observed under a confocal microscope.

4.8. Flow Cytometry Analysis

MCF-7 cells (1 × 10^6 cells) were cultured in a glass-bottomed confocal dish for 24 h to detect cellular apoptosis. Subsequently, the cells were treated with TPAPV-NIM-TSA@F127 (10 μM) and incubated for 6 h at 37 °C, followed by exposure to white light (40 mW/cm^2) for 15 min. After trypsinization, the cells were carefully extracted, centrifuged at 1500 rpm at 4 °C, and then washed with PBS. Subsequently, cells were stained with annexin V-FITC/PI (Thermo Fisher Scientific) according to the manufacturer's instructions, and flow cytometry was performed to assess apoptosis. For the control group, 1 × 10^6 MCF-7 cells were cultured in a glass-bottomed confocal dish and incubated with annexin V-FITC and PI according to the manufacturer's instructions (Thermo Fisher Scientific), followed by flow cytometry analysis.

4.9. Density Functional Theory (DFT/TDDFT) Calculations

All calculations were performed using the ADF 2023 program package at the B3LYP/DZP level of theory. Full geometry optimization was carried out for the molecule in the gas phase. Singlet and triplet excited states were obtained via the TDDFT formalism as implemented in ADF. Spin–orbit coupling (SOC) matrix elements were computed using the perturbative approach with the ZORA SOC Hamiltonian.

4.10. Animal Experiment

All animal experiments were performed at the animal center of Erciyes University in accordance with the guidelines of the Ethical Committee of Erciyes University (no. 24/216). To perform the in vivo PDT experiment, BALB/c mice aged ∼5 weeks were purchased from the animal center of Erciyes University (Erciyes University Hakan Çetinsaya Good Clinical Practice Center). All the mice were transferred to the experimental room and allowed to acclimate for 24 h. After that, they were randomly divided into three groups: PBS, dark, and light, with four mice per group (n = 4). Before the experiment, the hairs on the right flank of each mouse were removed, and all mice were infected with 4T1 tumor cells by subcutaneous injection of 1 × 10^6 4T1 cells into the right flank.

4.11. Blood Hemolysis Experiment

To examine the hemolytic effect of TPAPV-NIM-TSA@F127, fresh blood (1 mL) was collected from a healthy mouse. After that, the blood was centrifuged at 8000 rpm for 10 min at 4 °C to collect the red blood cells (RBCs), then washed twice with PBS. Subsequently, the RBCs were suspended in 7.0 mL of PBS and vortexed to get the RBC suspension. PBS served as a negative control, whereas deionized water (DI) functioned as a positive control. To perform the hemolysis experiment, 200 μL of RBC suspension was added to 800 μL of DI and PBS, serving as positive and negative controls, respectively. To assess the hemolytic effect of TPAPV-NIM-TSA@F127, 200 μL of red blood cell suspension was added to 800 μL of TPAPV-NIM-TSA@F127 solution in PBS to achieve a final concentration of 2.5 μM/mL of TPAPV-NIM-TSA@F127. A comparable methodology was employed for other concentrations of TPAPV-NIM-TSA@F127 (5.0 μM/mL, 10.0 μM/mL, 20.0 μM/mL, 30.0 μM/mL, 40.0 μM/mL, 50.0 μM/mL, 100.0 μM/mL, and 200.0 μM/mL). Following two hours of incubation at 37 °C, the hemolysis was measured at 577 nm using a microplate reader, and the hemolysis percentage was computed using the formula below

$$\text{Hemolysis (\%)} = \frac{A(\text{sample}) - A(\text{negative control})}{A(\text{positive control}) - A(\text{negative control})} \times 100$$

In this case, A represents the absorbance at 577 nm.

4.12. Hematoxylin and Eosin (H&E) Staining

On day 12, all mice were euthanized, and the vital organs (liver, spleen, kidneys, heart, and lungs) were collected from each group and stored in 10% formaldehyde at 4 °C for hematoxylin and eosin (H&E) staining. To perform H&E staining, the tissues were dehydrated through a graded series of alcohols, cleaned with xylene, and embedded in paraffin blocks. Then, 5 μm-thick sections were obtained using a microtome and stained with hematoxylin and eosin (H&E), and observed under a light microscope.

■ ASSOCIATED CONTENT

Supporting Information

The Supporting Information is available free of charge at https://pubs.acs.org/doi/10.1021/acsami.5c25184.

It includes zeta potential, molar absorption coefficient spectra, ROS detection via RB and Ce6, cytotoxicity results, ROS inhibitor data, photographs of the mice in the light group, hemolysis results, NMR spectra, and high-resolution mass spectra of the synthesized molecules (PDF)

■ AUTHOR INFORMATION

Corresponding Authors

Sayed Mir Sayed − *ERNAM—Nanotechnology Research and Application Center, Erciyes University, Kayseri 38039, Türkiye*; Email: sayed.mir.sayed5@gmail.com

Aysun Cetin − *Department of Medical Biochemistry, Institute of Health Sciences, Erciyes University, Kayseri 38039, Türkiye*; Email: aysuncetin@yahoo.com

Yavuz Nuri Ertas − *ERNAM—Nanotechnology Research and Application Center, Department of Biomedical Engineering, Genome and Stem Cell Center (GENKOK), and ERFARMA Drug Application and Research Center, Erciyes University, Kayseri 38039, Türkiye*; orcid.org/0000-0002-6791-7484; Email: yavuznuri@gmail.com

Authors

Zeeshan Tahir − *Department of Medical Biochemistry, Institute of Health Sciences, Erciyes University, Kayseri 38039, Türkiye*; orcid.org/0009-0001-1947-6151

Elif Lulek − *Department of Biomedical Engineering, Erciyes University, Kayseri 38039, Türkiye*

Zehra Busra Azizoglu − *Genome and Stem Cell Center (GENKOK), Erciyes University, Kayseri 38039, Türkiye*

https://doi.org/10.1021/acsami.5c25184
ACS Appl. Mater. Interfaces 2026, 18, 13516−13528

Gulce Yildiz − *Department of Histology and Embryology, Faculty of Medicine, Erciyes University, Kayseri 38280, Türkiye*

Esra Balcioglu − *Department of Histology and Embryology, Faculty of Medicine, Erciyes University, Kayseri 38280, Türkiye*

Complete contact information is available at: https://pubs.acs.org/10.1021/acsami.5c25184

Notes

The authors declare no competing financial interest.

■ ACKNOWLEDGMENTS

The authors acknowledge funding support from the Erciyes University Scientific Research Projects Coordination Unit (Project No: TDK-2025-14634) and 2232 International Fellowship for the Outstanding Researchers Program of TÜBİTAK (Project No: 121C157). Y.N.E. acknowledges support from the Turkish Academy of Sciences Distinguished Young Scientist Award (TÜBA-GEBİP) and Scientific and Technological Research Council of Türkiye (TÜBİTAK) Incentive Award.

■ REFERENCES

(1) Wang, S.; Zheng, R.; Li, J.; Zeng, H.; Li, L.; Chen, R.; Sun, K.; Han, B.; Bray, F.; Wei, W.; et al. Global, regional, and national lifetime risks of developing and dying from gastrointestinal cancers in 185 countries: a population-based systematic analysis of GLOBOCAN. *Lancet Gastroenterol. Hepatol.* **2024**, *9* (3), 229−237.

(2) Wei, L.; He, X.; Zhao, D.; Kandawa-Shultz, M.; Shao, G.; Wang, Y. Biotin-conjugated Ru (II) complexes with AIE characteristics as mitochondria-targeted photosensitizers for enhancing photodynamic therapy by disrupting cellular redox balance. *Eur. J. Med. Chem.* **2024**, *264*, 115985.

(3) Guo, S.; Tang, H.; Zhang, Y.; Wang, Z.; Tan, S. C. Recent advances in biomimetic aggregation-induced emission photosensitizers for photodynamic therapy and immunotherapy. *BMEMat* **2024**, *2* (3), No. e12076.

(4) Chai, Y.; Sun, Y.; Sheng, Z.; Zhu, Y.; Du, T.; Zhu, B.; Yu, H.; Dong, B.; Liu, Y.; Wang, H.-Y. Reversible pH-switchable NIR-II nanophotosensitizer for precise imaging and photodynamic therapy of tumors. *Acta Biomater.* **2024**, *188*, 315−328.

(5) Lu, M.; Huang, M.; Chen, J.; Xu, X.; Liu, S.; Wang, W.; Si, W.; Huang, X.; Dong, X. Subcellular organelle targeted tumor phototherapy. *Coord. Chem. Rev.* **2025**, *535*, 216635.

(6) Colak, B.; Ertas, Y. N. Implantable 3D-Printed Alginate Scaffolds with Bismuth Sulfide Nanoparticles for the Treatment of Local Breast Cancer via Enhanced Radiotherapy. *ACS Appl. Mater. Interfaces* **2024**, *16* (13), 15718−15729.

(7) Yaray, K.; Norbakhsh, A.; Rashidzadeh, H.; Mohammadi, A.; Mozafari, F.; Ghaffarlou, M.; Mousazadeh, N.; Ghaderzadeh, R.; Ghorbani, Y.; Nasehi, L.; et al. Chemoradiation therapy of 4T1 cancer cells with methotrexate conjugated platinum nanoparticles under X-Ray irradiation. *Inorg. Chem. Commun.* **2023**, *150*, 110457.

(8) Yang, Y.; Zhang, Y.; Zhou, S.; Fang, X.; Zhang, X.; Wei, W.; Huang, G.; Wu, C. Self-Assembled Nanobody-Albumin Platform with Dye Encapsulation for NIR-II Imaging-Guided Photodynamic Therapy. *ACS Appl. Mater. Interfaces* **2025**, *17* (31), 44249−44262.

(9) Colak, B.; Cihan, M. C.; Ertas, Y. N. 3D-Printed, Implantable Alginate/CuS Nanoparticle Scaffolds for Local Tumor Treatment via Synergistic Photothermal, Photodynamic, and Chemodynamic Therapy. *ACS Appl. Nano Mater.* **2023**, *6* (17), 16076−16085.

(10) Miao, J. F.; Yao, G. X.; Huo, Y. Y.; Wang, B. B.; Zhao, W.; Guo, W. Constructing Heavy-Atom-Free Photosensitizers for Hypoxic Tumor Phototherapy Based on Donor-Excited Photoinduced Electron-Transfer-Driven Type-I and Type-II Mechanisms. *ACS Appl. Mater. Interfaces* **2024**, *16* (31), 40428−40443.

(11) Lu, S. L.; Yin, D. F.; Wang, X. J.; Han, M.; Wang, Z.; Zhang, Y. R.; Ma, X. S.; Yang, Y.; Gao, D. M.; Wang, Z. G. Metabolizable Photosensitizers with Aggregation-Induced Emission for Photodynamic Cancer Therapy. *ACS Appl. Nano Mater.* **2025**, *8* (41), 19852−19865.

(12) Yang, X.; Wang, X.; Zhang, X.; Zhang, J.; Lam, J. W.; Sun, H.; Yang, J.; Liang, Y.; Tang, B. Z. Donor−Acceptor Modulating of Ionic AIE Photosensitizers for Enhanced ROS Generation and NIR-II Emission. *Adv. Mater.* **2024**, *36* (28), 2402182.

(13) Sayed, S. M.; Xu, K.-F.; Jia, H.-R.; Yin, F.-F.; Ma, L.; Zhang, X.; Khan, A.; Ma, Q.; Wu, F.-G.; Lu, X. Naphthalimide-based multifunctional AIEgens: Selective, fast, and wash-free fluorescence tracking and identification of Gram-positive bacteria. *Anal. Chim. Acta* **2021**, *1146*, 41−52.

(14) Sayed, S. M.; Jia, H.-R.; Jiang, Y.-W.; Zhu, Y.-X.; Ma, L.; Yin, F.; Hussain, I.; Khan, A.; Ma, Q.; Wu, F.-G.; Lu, X. Photostable AIE probes for wash-free, ultrafast, and high-quality plasma membrane staining. *J. Mater. Chem. B* **2021**, *9* (21), 4303−4308.

(15) Wang, A.; Liu, K. X.; Wang, Q. D.; Zhang, Y. M.; Chen, H. N.; Li, W. P.; Jiang, X. Y. Orthogonal Holographic and Multicolor Fluorescent Images via Aggregation Caused Quenching and Aggregation Induced Emission Nanoparticles with Forster Resonance Energy Transfer. *ACS Nano* **2025**, *19* (35), 31768−31779.

(16) Zhao, W.; Wang, L. Q.; Zhang, M. H.; Liu, Z. Q.; Wu, C. B.; Pan, X.; Huang, Z. W.; Lu, C.; Quan, G. L. Photodynamic therapy for cancer: mechanisms, photosensitizers, nanocarriers, and clinical studies. *MedComm* **2024**, *5* (7), No. e603.

(17) Luo, J.; Xie, Z.; Lam, J. W.; Cheng, L.; Tang, B. Z.; Chen, H.; Qiu, C.; Kwok, H. S.; Zhan, X.; Liu, Y.; et al. Aggregation-induced emission of 1-methyl-1, 2, 3, 4, 5-pentaphenylsilole. *Chem. Commun.* **2001**, No. 18, 1740−1741.

(18) Wang, H.; Li, Q.; Alam, P.; Bai, H.; Bhalla, V.; Bryce, M. R.; Cao, M.; Chen, C.; Chen, S.; Chen, X.; et al. Aggregation-induced emission (AIE), life and health. *ACS Nano* **2023**, *17* (15), 14347−14405.

(19) Dong, M.-J.; Wang, X.; Yang, J. L.; Peng, W. H.; Yang, S. S.; Xiang, Q.; Zheng, J.; Dong, H. F.; Zhang, X. J. Spatiotemporal organelle delivery and activation of type I AIE photosensitizers and siRNA for near-infrared fluorescence image-guided immunotherapy. *Biomaterials* **2026**, *328*, 123827.

(20) Ma, H.; Li, R. X.; Meng, H. B.; Tian, M.; Zhang, X. H.; Liu, Y. L.; Li, L.; Yuan, J. Y.; Wei, Y. A Versatile Theranostic Nanoplatform with Aggregation-Induced Emission Properties: Fluorescence Monitoring, Cellular Organelle Targeting, and Image-Guided Photodynamic Therapy. *Small* **2023**, *19* (21), 2204778.

(21) Chen, W.-H.; Luo, G. F.; Zhang, X. Z. Recent advances in subcellular targeted cancer therapy based on functional materials. *Adv. Mater.* **2019**, *31* (3), 1802725.

(22) Zhu, Y.; Zhang, R.; Cai, X. M.; Zhang, L.; Wu, B.; Tan, H.; Zhou, K.; Wang, H.; Liu, Y.; Luo, Y.; et al. Acceptor Elongation Boosted Intersystem Crossing Affords Efficient NIR Type-I and AIE-Active Photosensitizers for Targeting Ferroptosis-Based Cancer Therapy. *Adv. Healthcare Mater.* **2025**, *14* (7), 2404505.

(23) Du, X.; Huang, S.; Lin, Z.; Chen, G.; Jiang, Y.; Zhang, H. Organelle-targeted small molecular photosensitizers for enhanced photodynamic therapy: a minireview for recent advances and potential applications. *Chem. Commun.* **2025**, *61* (40), 7236−7252.

(24) Wang, R.; Li, X.; Yoon, J. Organelle-targeted photosensitizers for precision photodynamic therapy. *ACS Appl. Mater. Interfaces* **2021**, *13* (17), 19543−19571.

(25) Zhao, M. Y.; Zhang, W. G.; Fan, M. Z.; Xu, Z. R.; Jiang, Y. H.; Li, Z. Z.; Zhai, P.; Zhang, X. M.; Chen, T.; Zhang, Y. B.; et al. AIEgen Photosensitizer-Loaded Silica Nanoparticles for Lysosomes-Targeting Photodynamic Therapy in Tumor. *ACS Appl. Nano Mater.* **2024**, *7* (20), 23504−23512.

(26) Miao, Z.; Li, J.; Zeng, S.; Lv, Y.; Jia, S.; Ding, D.; Li, W.; Liu, Q. Endoplasmic reticulum-targeting AIE photosensitizers to boost

immunogenic cell death for immunotherapy of bladder carcinoma. *ACS Appl. Mater. Interfaces* **2024**, *16* (1), 245−260.
(27) Yang, Z. Z.; Teng, Y. L.; Lin, M.; Peng, Y. W.; Du, Y. T.; Sun, Q.; Gao, D. T.; Yuan, Q.; Zhou, Y.; Yang, Y. L.; et al. Reinforced Immunogenic Endoplasmic Reticulum Stress and Oxidative Stress via an Orchestrated Nanophotoinducer to Boost Cancer Photoimmunotherapy. *ACS Nano* **2024**, *18* (9), 7267−7286.
(28) Yang, Y.; Lu, D. F.; Wang, M. H.; Liu, G. J.; Feng, Y.; Ren, Y. B.; Sun, X. O.; Chen, Z. Q.; Wang, Z. Endoplasmic reticulum stress and the unfolded protein response: emerging regulators in progression of traumatic brain injury. *Cell Death Dis.* **2024**, *15* (2), 156.
(29) Liu, Y.; Xu, C. L.; Gu, R. J.; Han, R. Q.; Li, Z. Y.; Xu, X. R. Endoplasmic reticulum stress in diseases. *MedComm* **2024**, *5* (9), No. e701.
(30) Wu, Y.; Chen, X.; Zhu, L.; Wang, D.; Li, X.; Song, J.; Wang, D.; Yu, X.; Li, Y.; Tang, B. Z. Endoplasmic reticulum-targeted aggregation-induced emission luminogen for synergetic tumor ablation with glibenclamide. *ACS Appl. Mater. Interfaces* **2023**, *15* (44), 50821−50835.
(31) Huang, P.-Y.; Liang, S. Y.; Xiang, Y.; Li, M. R.; Wang, M. R.; Liu, L. H. Endoplasmic Reticulum-Targeting Self-Assembly Nanosheets Promote Autophagy and Regulate Immunosuppressive Tumor Microenvironment for Efficient Photodynamic Immunotherapy. *Small* **2024**, *20* (25), 2311056.
(32) Zhao, X.; Ma, H.; Chen, J.; Zhang, F.; Jia, X.; Xue, J. An epidermal growth factor receptor-targeted and endoplasmic reticulum-localized organic photosensitizer toward photodynamic anticancer therapy. *Eur. J. Med. Chem.* **2019**, *182*, 111625.
(33) Hou, J.-T.; Kim, H. S.; Duan, C.; Ji, M. S.; Wang, S.; Zeng, L.; Ren, W. X.; Kim, J. S. A ratiometric fluorescent probe for detecting hypochlorite in the endoplasmic reticulum. *Chem. Commun.* **2019**, *55* (17), 2533−2536.
(34) Li, X.; Yang, L.; He, B.; Li, D.; Lei, C.; Li, N.; Zhao, N. An endoplasmic reticulum-targeted NIR-II type I AIE photosensitiser for triggering pyroptosis. *Chem. Commun.* **2025**, *61* (85), 16580−16583.
(35) Fan, Y.; Zhang, F.; Hao, Y.; Chen, L.; Zhou, Q.; Zeng, H.; Song, Y.; Guo, Z.; Peng, X.; Ge, G. Fluorogenic Probes for Functional Imaging of Endoplasmic Reticulum-Resident Proteins: from Molecular Engineering to Biomedical Applications. *Adv. Funct. Mater.* **2025**, *35* (9), 2416057.
(36) Ma, Y.; Han, M.; Zhu, H.; Cui, F.; Qiao, Y.; Yin, Y.; Zhao, X.; Xi, R.; Meng, M. Dual-Modulation Design to Develop ER-Targeting NIR Pyroptosis Inducers with Type I PDT Efficacy and Amplified Antitumor Immunity. *Anal. Chem.* **2025**, *97* (23), 12338−12346.
(37) Kaur, G.; Singh, I.; Tandon, N.; Tandon, R.; Bhat, A. A. 1,8-Naphthalimide-Based Chemosensors: A Promising Strategy for Detection of Metal Ions in Environmental and Biological Systems. *ChemistrySelect* **2023**, *8* (44), No. e202301661.
(38) Jia, T.; Fu, C.; Huang, C.; Yang, H.; Jia, N. Highly sensitive naphthalimide-based fluorescence polarization probe for detecting cancer cells. *ACS Appl. Mater. Interfaces* **2015**, *7* (18), 10013−10021.
(39) Xu, H.; Xiao, Y.; Liu, Y.-G.; Sun, W. Research Progress on Naphthalimide Fluorescent Probes. *Adv. Sens. Res.* **2024**, *3* (2), 2300032.
(40) Peng, M.; Wei, H.; Wang, Q.; Guan, J.; Yin, M. Naphthalimide Nanoprobe with Enhanced Electron-Withdrawing Ability and Large Stokes Shift for NIR-II Fluorescence Imaging-Guided Phototheranostics. *ACS Appl. Mater. Interfaces* **2025**, *17* (8), 11742−11751.
(41) Shen, R.; Bai, J.; Qian, Y. A mitochondria-targeted fluorescent dye naphthalimide-thioether-cyanine for NIR-activated photodynamic treatment of cancer cells. *J. Mater. Chem. B* **2021**, *9* (10), 2462−2468.
(42) Sha, Q.; Li, X.; Gu, X.; Yuan, T.; Hua, J. A self-aggregated thermally activated delayed fluorescence nanoprobe for HClO imaging and activatable photodynamic therapy. *Talanta* **2025**, *286*, 127570.
(43) Niu, H.; Liu, Y.; Wang, Y.; Yang, Y.; Wang, G.; James, T. D.; Sessler, J. L.; Zhang, H. Photochemical and biological dual-effects enhance the inhibition of photosensitizers for tumour growth. *Chem. Sci.* **2024**, *15* (20), 7757−7766.
(44) Niu, H.; Wang, S. N.; Liu, Y.; Ma, N. N.; Cheng, S. W.; Feng, B. D.; Jeong, H.; Yang, Y. G.; Wang, G.; James, T. D.; et al. Naphthalimide-Based Type-I Nano-Photosensitizers for Enhanced Antitumor Photodynamic Therapy: H2S Synergistically Regulates PeT and Self-Assembly. *Angew. Chem., Int. Ed.* **2025**, *64* (48), No. e202512150.
(45) Feng, J.; Jian, X.; Jiang, G.; Wang, J. Charged aggregation-induced emission luminogens for bioimaging and phototherapy. *Luminescence* **2024**, *39* (1), No. e4669.
(46) Yang, J.; Griffin, A.; Qiang, Z.; Ren, J. Organelle-targeted therapies: a comprehensive review on system design for enabling precision oncology. *Signal Transduction Targeted Ther.* **2022**, *7* (1), 379.
(47) Hong Luo, G.; Xu, T. Z.; Li, X.; Jiang, W.; Duo, Y. H.; Tang, B. Z. Cellular organelle-targeted smart AIEgens in tumor detection, imaging and therapeutics. *Coord. Chem. Rev.* **2022**, *462*, 214508.
(48) Sayed, S. M.; Li, X.-F.; Jia, H.-R.; Durrani, S.; Wu, F.-G.; Lu, X. A dibenzothiophene core-based small-molecule AIE probe for wash-free and selective staining of lipid droplets in live mammalian and fungal cells. *Sens. Actuators, B* **2021**, *343*, 130128.
(49) Zhang, S.; Yang, W.; Lu, X.; Zhang, X.; Pan, Z.; Qu, D.-H.; Mei, D.; Mei, J.; Tian, H. Near-infrared AIEgens with high singlet-oxygen yields for mitochondria-specific imaging and antitumor photodynamic therapy. *Chem. Sci.* **2023**, *14* (25), 7076−7085.

https://doi.org/10.1021/acsami.5c25184
ACS Appl. Mater. Interfaces 2026, 18, 13516−13528